Perfect isolation of π-conjugated molecules on inorganic surfaces with [1]rotaxane structure for enhancing electrical properties

Sheng-Ying Chou
The University of Tokyo
Hiroshi Masai
University of Tokyo
Masaya Otani
The University of Tokyo
Gentaro Sakamoto
Osaka City Univeristy
Yusuke Yamada
Osaka City Univeristy
Yusuke Kinoshita
Ritsumeikan University
Hitoshi Tamiaki
Ritsumeikan University https://orcid.org/0000-0003-4797-0349
Takayoshi Katase
Hokkaido University
Hiromichi Ohta
Hokkaido University https://orcid.org/0000-0001-7013-0343
Tomoki Kondo
Kyoto University
Akinobu Nakada
Kyoto University https://orcid.org/0000-0001-6670-5044
Ryu Abe
Kyoto University
Takahisa Tanaka
University of Tokyo
Ken Uchida
University of Tokyo
Jun Terao (cterao@g.ecc.u-tokyo.ac.jp)
The University of Tokyo

Article

Keywords: π-conjugated molecules, [1]rotaxane structure, inorganic surfaces

Posted Date: May 13th, 2021

DOI: https://doi.org/10.21203/rs.3.rs-464533/v1

Perfect isolation of π-conjugated molecules on inorganic surfaces with [1]rotaxane structure for enhancing electrical properties

Sheng-Ying Chou,[1] Hiroshi Masai,[1] Masaya Otani,[1] Gentaro Sakamoto,[2] Yusuke Yamada,[2] Yusuke Kinoshita,[3] Hitoshi Tamiaki,[3] Takayoshi Katase,[4,7] Hiromichi Ohta,[4] Tomoki Kondo,[5] Akinobu Nakada,[5,8] Ryu Abe,[5] Takahisa Tanaka,[6] Ken Uchida,[6] Jun Terao[1*]

Affiliations

[1] Department of Basic Science, Graduate School of Arts and Sciences, The University of Tokyo, Meguro-ku, Tokyo, Japan

Sheng-Ying Chou, Hiroshi Masai (orcid.org/0000-0002-4231-1320), Masaya Otani & Jun Terao (orcid.org/0000-0003-1867-791X)

[2] Department of Applied Chemistry and Bioengineering, Graduate School of Engineering, Osaka City University, Sumiyoshi-ku, Osaka, Japan

Gentaro Sakamoto & Yusuke Yamada (orcid.org/0000-0003-0088-0549)

[3] Department of Applied Chemistry, Graduate School of Life Sciences, Ritsumeikan University, Kusatsu-shi, Shiga, Japan

Yusuke Kinoshita (orcid.org/0000-0001-7681-2644) & Hitoshi Tamiaki (orcid.org/0000-0003-4797-0349)

[4] Research Institute for Electronic Science, Hokkaido University, Kita-ku, Sapporo, Japan

Takayoshi Katase (orcid.org/0000-0002-2593-7487) & Hiromichi Ohta (orcid.org/0000-0001-7013-0343)

[5] Department of Energy and Hydrocarbon Chemistry, Graduate School of Engineering, Kyoto University, Nishikyo-ku, Kyoto, Japan

Tomoki Kondo, Akinobu Nakada (orcid.org/0000-0001-6670-5044) & Ryu Abe (orcid.org/0000-0001-8592-076X)

[6] Department of Materials Engineering, The University of Tokyo, Bunkyo-ku, Tokyo, Japan

Takahisa Tanaka & Ken Uchida (orcid.org/0000-0001-8307-5232)

[7] Laboratory for Materials and Structures, Institute of Innovative Research, Tokyo Institute of Technology, Midori-ku, Yokohama, Japan

Takayoshi Katase

[8] Department of Applied Chemistry, Faculty of Science and Engineering, Chuo University, Tokyo, Japan; Precursory Research for Embryonic Science and Technology (PRESTO), Japan Science and Technology Agency (JST), Kawaguchi, Saitama, Japan

Akinobu Nakada

Contributions

H.M. and J.T. designed and directed the project. S.-Y. C. performed the synthetic experiments and collected the central data. O.M. collaborated with S.-Y. C. to investigate the interfacial charge transfer. G.S. and Y.Y. performed and interpreted the electrocatalysis. Y.K. and H.T. synthesized the Co-catalyst. T.Ka. and H.O. manufactured the single-crystalline ITO substrates. T.Ko., A.K. and R.A. investigated the optical analyses of the modified ITO substrates. T.T. and K.U. performed and analyzed XPS. S.-Y. C. and H.M. wrote the manuscript. All authors have approved the manuscript.

Corresponding author

Correspondence to: Jun Terao

orcid.org/0000-0003-1867-791X

Email: cterao@g.ecc.u-tokyo.ac.jp

Abstract

π-Conjugated molecules have been utilized to functionalize inorganic surfaces to form organic–inorganic hybrid materials. However, the intrinsically strong π–π interaction results in undesirable aggregations on the inorganic surface, thereby disturbing the charge transfer through the organic–inorganic interface. In this

study, a new strategy was developed using insulated π-conjugated molecules bearing a [1]rotaxane structure, where the π-conjugation was covered with covalently linked permethylated α-cyclodextrins. Aggregation-free immobilization was achieved on an inorganic surface by using insulated molecules to suppress intermolecular interaction. In the presence of these insulated molecules, the hybrid interface displayed excellent interfacial electrical properties. Moreover, the functionalized hybrid surface was utilized as an electrocatalyst to produce hydrogen peroxide using a Co(II)–chlorin complex, wherein the catalytic efficiency was improved dramatically by utilizing insulated molecules as bridging moieties at the interface. These results demonstrate that the insulation of π-conjugated molecules is a powerful strategy for modifying inorganic surfaces.

Introduction

Immobilization of organic molecules onto inorganic surfaces synergistically integrates the features of both components, resulting in exceptional material properties.[1,2] In particular, π-conjugated molecules, which possess unique optical and electrical properties, have been utilized for diverse organic–inorganic hybrid devices such as memory devices, solar cells, and biosensors.[3–5] Particularly, in the case of electrical devices, the high molecular modification density and high charge-transfer efficiency at the interface, which are governed by the morphology of the surface organic components, are critical to the device performance.[6,7] Conventional surface modifications of inorganic materials using π-conjugated molecules have been achieved via self-assembled monolayers (SAMs),[8] covalent bond formations,[9,10] and depositions.[11,12] However, these classical methods are only suitable for simple and limited conjugated molecules (i.e., unexpanded π-conjugation) to provide uniform and ordered hybrid interfaces. Although π-expanded conjugated molecules offer high functionalities for such electrical devices, they readily form objectionable aggregation on surfaces, owing to their strong π–π interaction (Fig. 1a).[13–15] This aggregation induces disordering and large protrusions on the surface; therefore, rather than direct injection into the inorganic materials, unanticipated charge transfer between the adjacent molecules occurs on the surface of these materials. This decreases the charge-transfer efficiency of the material. Thus, π-expanded conjugated

molecules for electrical devices result in undesirable aggregation, limiting the improvement of the functional device performance. Paving the optimum conductive pathways at the interface by inhibiting π-aggregation is therefore critical to improve the material performance, especially for electrical devices with π-expanded conjugated molecules.

To suppress π-aggregation, an isolated environment is typically created around π-expanded conjugated molecules on the material surface by utilizing aliphatic compounds. Mixed SAM methods, where the conjugated molecules are diluted in a non-conjugated molecular monolayer, provide an isolated environment around the π-conjugation.[16–18] However, such methods require a low π-conjugation composition ratio, which is disadvantageous for electric devices. On the other hand, increasing the concentration of π-conjugated molecules induces the formation of aggregation structures on the surface of the material. Similarly, some π-conjugated systems bearing bulky side chains to suppress π–π interaction afford uniform surface monolayers.[19,20] However, such ordered systems are attributed to the appropriate surface molecular interaction, and further π-expansion would also result in their aggregation. Overall, except for low-concentration immobilization, most π-expanded aromatic compounds cannot be immobilized on surfaces without aggregation. Accordingly, high-density uniform immobilization of π-expanded functional conjugation at the hybrid interface remains a challenging target.

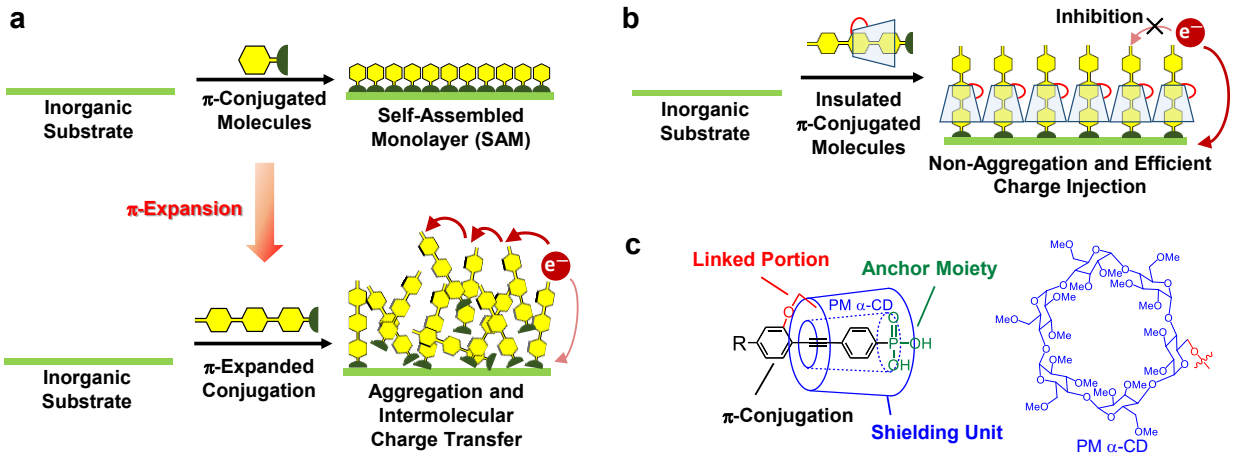

Fig. 1 Conceptual illustration of modification of inorganic surface using π-conjugated molecules. **a** SAMs constructed by unexpanded π-conjugated molecules (top) and intermolecular charge transfer caused

by undesirable aggregation due to strong aromatic interaction derived from the expansion of the π-conjugated backbone (bottom). **b** Non-aggregation and efficient charge injection because of π–π interaction and intermolecular charge-transfer inhibition using [1]rotaxane structure. **c** Molecular design of the conjugated molecules bearing the [1]rotaxane structure for surface immobilization.

Recently, rotaxane structures have gained importance as a promising method to inhibit π–π interaction.[21,22] The cyclic molecules efficiently cover the π-conjugated axles and inhibit unfavorable π-aggregation.[23,24] In particular, pseudorotaxanes, in which cyclic and axis molecules dynamically form threading structures,[25,26] have been utilized for hybrid modification because of their facile in situ preparation.[27] However, owing to their lack of stoppers, pseudorotaxanes can dynamically dissociate to form irregular structures on the hybrid interfaces, including aggregated π-conjugated molecules and empty cyclic molecules. These unclear and aggregated structures decrease the electrical properties of the hybrid interface. Consequently, examples of hybrid materials utilizing pseudorotaxanes to improve the electrical performance in terms of effective electron injections at the hybrid interface have rarely been reported.[28–31] Therefore, a new strategy for highly advanced molecular designing of π-expanded conjugated molecules, to attain fine interface immobilization, would create new platforms toward further growth in this field of nanoscience.

To address these concerns, we introduced the [1]rotaxane strategy (Figs. 1b and 1c).[32–36] In contrast to common rotaxane structures, [1]rotaxane structures prevent macrocycles from dissociating, without any bulky stopper units in the rotaxanes. The defect-free insulation improves their conversion ratio on the axles and ensures that the conjugated molecules are highly insulated. As a result, the physical properties derived from their conjugation are preserved from the effect of their π–π interaction, even in the solid state, because of the high proportion of covering structures.[37–41] Their advantage as highly protected structures inspired the design of a novel insulated conjugated molecule for immobilization on inorganic surfaces. The defect-free structures contribute non-aggregation structures with high density and uniform π-expanded conjugation immobilization at the hybrid interface to inhibit intermolecular charge transfer. Moreover, the finely

controlled interface at the molecular scale provides high-performance electrical devices via efficient charge transfer through each π-conjugated backbone. In this study, we synthesized an insulated conjugated molecule to achieve independent immobilization on inorganic substrates. The molecule comprises phenylene-ethynylene (PE)-based π-conjugation covered by a linked permethylated α-cyclodextrin (PM α–CD) as the shielding unit, and displays high solubility in organic solvents together with a deep cavity (Fig. 1c). As an anchoring moiety to the substrates, phosphonic acid was directly introduced at the end of the conjugated section to allow strong interaction and to transfer the charge to various metal oxide substrates[9,42] such as indium tin oxide (ITO) and fluorine-doped tin oxide (FTO), which are utilized as electrodes in electrical devices. The insulation effects were investigated to clarify the high-degree independency and excellent electrical properties on the hybrid interface compared to those on the uninsulated counterparts, owing to the inhibition of intermolecular interactions by three-dimensional encapsulation. In addition, the hybrid system based on [1]rotaxanes was applied to electrocatalysis, revealing marked improvement in the catalytic efficiency. The results demonstrated that enhanced charge-transfer and catalytic efficiencies were achieved because the [1]rotaxane strategy efficiently isolated the π-conjugated molecules to inhibit π–π interaction. This strategy shows great potential for application to various electric devices.

Results

Synthesis of Insulated Junction Molecules

The immobilization behavior of cyclic-insulated molecules was investigated using insulated conjugated molecule **3**. Precursor **1** bearing PM α–CD and terminal ethyl-protected phosphonic acid was prepared according to previously reported procedures.[43] Moreover, **1** was converted into the corresponding insulated structure **2** quantitatively by hydrophobic–hydrophilic interactions in a heated (60 °C) high-polarity solvent ($MeOH/H_2O$ = 1:1). This was followed by deprotection of the ethyl ether groups in **1** and **2** using trimethylsilyl bromide (TMSBr) and triethylamine (TEA) in dichloromethane (CH_2Cl_2) to obtain

144 the uninsulated and insulated phosphonic acid-derived molecules **3'** and **3**, respectively, (Fig. 2a). The high
145 activation barrier for the threading/dethreading transformations[44] was confirmed in previous works[45–48] and
146 hence, heating the solvent mixture was essential for converting **1** to **2** and vice versa. Thus, these structures
147 displayed kinetic stability at ambient temperature. The high kinetic stability at room temperature allowed
148 the selective preparation of **3'** and **3** via deprotection of the ethyl ether groups in **1** and **2**, respectively. In
149 the ^{1}H NMR spectra (Fig. 2b), the chemical shifts in the aromatic region of **3** were clearly shifted downfield
150 relative to those of the uninsulated counterpart **3'**, owing to deshielding by the threading structure.[46] The
151 loss of ethyl proton signals in the aliphatic region confirmed successful deprotection without any unwanted
152 changes to the insulated/uninsulated structures. In addition, insulated molecule **3** was kinetically stable even
153 in low-polarity solvents, in which the uninsulated structures are thermodynamically favored. Indeed, the
154 insulation remained intact after storage in $CHCl_3$ at room temperature for one day.

155 Insulation Effects on the Surface Morphology

156 The insulation effects on the molecular morphologies of **3'** and **3** after their immobilization on the
157 metal oxide surface were next investigated. To establish whether the surface protrusions were created by
158 the immobilized species or the surface substrate itself, commercially unavailable single-crystalline ITO
159 substrates with ultra-flat surfaces (root mean square roughness, <0.2 nm), fabricated by pulsed laser
160 deposition on single crystal YSZ plate, were utilized.[49,50] Compared to those of amorphous ITO, the
161 individual heights of **3'** and **3** on the single-crystalline ITO surfaces were easily and correctly analyzed in
162 detail using atomic force microscopy (AFM). The crystalline ITO substrates were modified by dipping into
163 a low-concentration (50 μM) MeOH solution of **3'** or **3**. The low concentration prevented high-density
164 adsorption of the conjugated molecules on the ITO surface, thereby enabling the analysis of the individual
165 height of each adsorption species by AFM. Consequently, the AFM image revealed that the single-
166 crystalline ITO substrate, which showed a regular step-and-terrace structure, similar to that reported by
167 Ohta et al.,[49,50] was modified by the numerous protrusions of insulated conjugated molecule **3** (Fig. 2c). The
168 height distribution of this molecule on the single-crystalline ITO surface mostly ranged from 0.9 to 1.9 nm[51]

(Fig. 2e), which approached the calculated length of **3** (1.7 nm; Fig. S2). This indicated that the observed structure was the attached single molecule. The formation of huge protrusions, owing to undesirable aggregation of the uninsulated conjugated molecule **3'** on the single-crystalline ITO surface, was observed (Figs. 2d and 2f). In the histogram of immobilized **3'** (Fig. 2f, inset), the height frequency exceeded 2 nm, which was considered as aggregation, in more than 10% of the graph. This indicated that for uninsulated **3'**, surface aggregation occurred even when a low-concentration solution was utilized for surface modification. Indeed, although uninsulated **3'** possessed PM α–CD as a bulky side chain, the strong intermolecular interactions between the expanded conjugation resulted in an unfavorable aggregated structure on the ITO substrate.

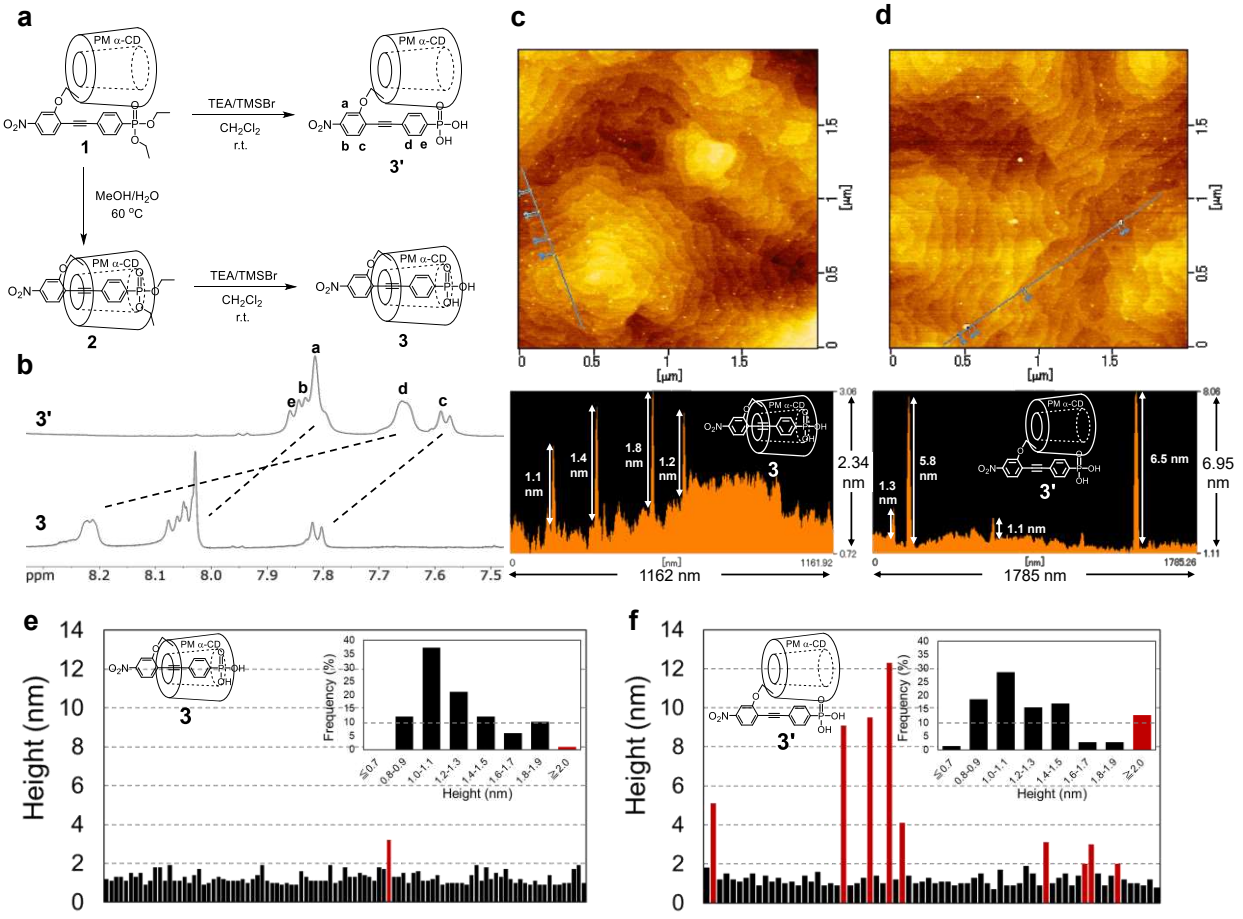

Fig. 2 Synthesis of insulated/uninsulated molecules and morphology of the modified single-crystalline ITO substrates. a Synthetic route of insulated/uninsulated molecules (**3**/**3'**). **b** Aromatic region in the ^{1}H

NMR spectra of (top) **3'** and (bottom) **3**. AFM images of the single-crystalline ITO substrates modified by **c 3** and **d 3'** with the plan views and cross-sectional profiles. Height of each protrusion of **e** immobilized **3** (99 counts; inset: histogram of height analyses) and **f** immobilized **3'** (70 counts; inset: histogram of height analyses) in the AFM image.

Insulation Effects on the Interface Electronic Properties

To analyze the electrical properties of the immobilized molecules, **4** and **4'** bearing redox-active ferrocene units were next prepared (Scheme S3). The surface coverage concentration (Γ) and other electrical properties were then determined using cyclic voltammetry. The experiment for calculating the Γ values was carried out in a 0.1 M solution of tetrabutylammonium hexafluorophosphate ($TBAPF_6$) in CH_2Cl_2. Γ values were then obtained from the cyclic voltammograms using the formula:[52]

$$\Gamma = Q/nFA \quad (1)$$

where Q is the charge obtained by integrating the anodic peak in the cyclic voltammogram (gray area in Fig. 3a), n is the number of electrons transferred during the redox process (n = 1 for **4** and **4'**), F is the Faraday constant ($F = 9.65\times10^4$ s A mol^{-1}), and A is the immersed area of the electrode. The maximum Γ value of **4** was observed when the ITO substrate was immersed into a 1000 μM MeOH solution of **4** (Table S2). Subsequently, the ITO substrate was also immersed into a 1000 μM MeOH solution of **4'**. The Γ values of insulated **4** and uninsulated **4'** are summarized in Table S3. The Γ value of **4'** was approximately twice that of **4** because of the immense protrusions observed on the AFM images, which were created by aggregation of uninsulated **4'** on ITO (Fig. 3c). The cyclic voltammograms of the **4**-modified ITO electrode were next recorded at different scan rates. The plot of peak current versus scan rate (Figs. 3b and S3a) revealed a linear relationship, confirming that **4** was adsorbed on the electrode surface. The peak current corresponded to the current from the electrode-adsorbed redox species according to the formula:[53,54]

$$i_p = \frac{n^2F^2}{4RT}\nu A\Gamma \quad (2)$$

where i_p is the peak current and v is the scan rate. In addition,there was negligible change in the Γ value of immobilized **4** when the potential sweep was repeated 25 times (Figs. S4a and S4b). This indicated that the modified surface prepared utilizing the insulated molecule **4** displayed significant redox durability.

In the cyclic voltammograms, the separation between the anodic and cathodic peaks of the redox-active species immobilized on the electrode surface is designated as 0 mV under ideal reversible conditions.[55] At a scan rate of 100 mV s^{-1}, the peak-to-peak separation was 3 mV for both immobilized **4** (Fig. 3a) and immobilized **4'** (Fig. S3b). This value is small enough to be in excellent agreement with the ideal value for the reversible response of a surface-adsorbed species. Moreover, the value of the full width at half maximum (FWHM) in the cyclic voltammograms was utilized to assess the immobilized molecules at the point of the electrostatic interaction with the neighboring species,[53] i.e., as the repulsion forces were dominant, the redox peak was wider than the ideal width (90.6/n mV at 25 °C, n = 1 for **4** and **4'**), while when the attraction forces were dominant, the redox peak became narrower than the ideal width.[56] Moreover, while the FWHM value of immobilized **4'** (77 mV) was smaller than the ideal value (Fig. S3b), that of immobilized **4** (88 mV) approached the ideal value (Fig. 3a). The smaller FWHM of **4'** on the ITO surface was attributed to the electrostatic interaction between neighboring molecules due to unwanted aggregation. On the other hand, the intermolecular interaction between the molecules of **4** on the ITO surface was efficiently inhibited by the [1]rotaxane structure, providing isolated π-conjugated cores even at the organic–inorganic interface.

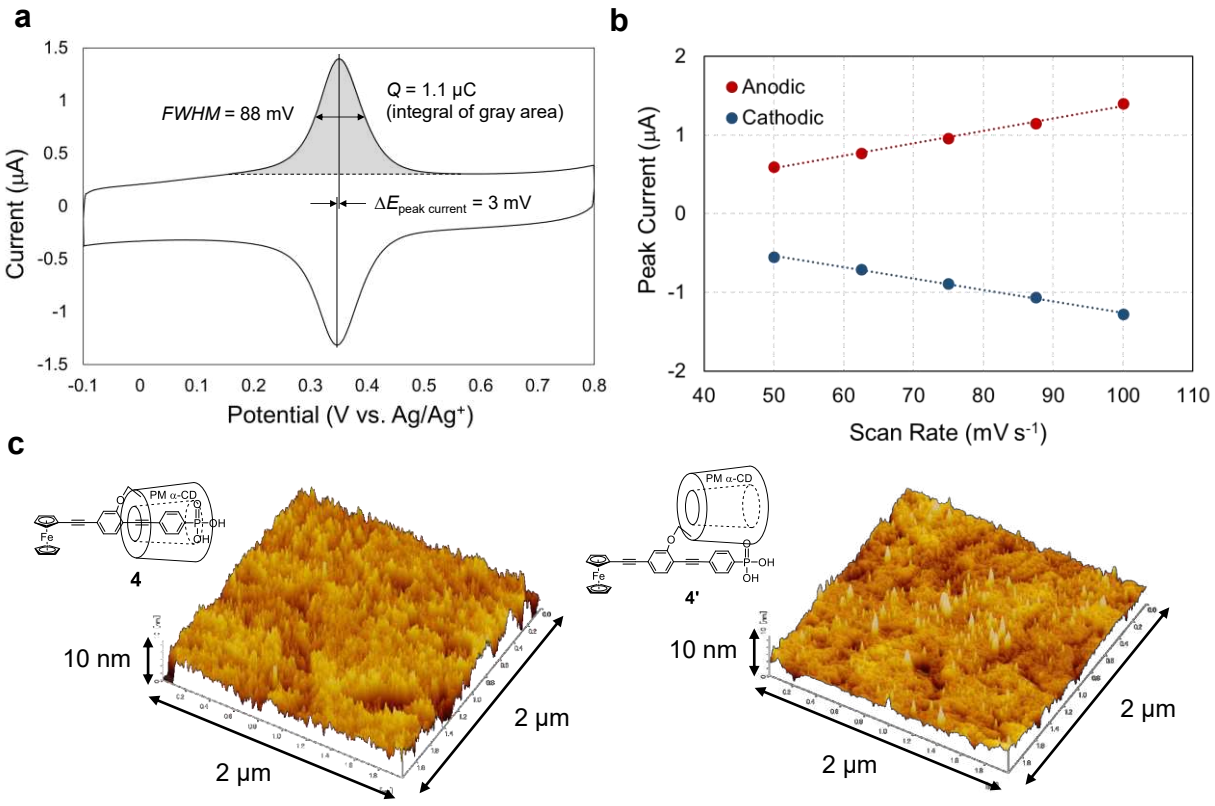

222

223 **Fig. 3 Interfacial electronic properties and morphology of modified ITO substrates. a** Cyclic
224 voltammogram of immobilized **4** at a scan rate of 100 mV s^{-1}. Conditions: 100 mM CH_2Cl_2 solution of
225 $TBAPF_6$. **b** Plot of anodic and cathodic peak currents of immobilized **4** versus the scan rates. **c** AFM images
226 of the ITO substrate modified with (left) **4** and (right) **4'**.

227

228 The increase in peak-to-peak separation with faster scan rates was attributed to the slow charge
229 transfer between the ITO and immobilized redox-active species.[57,58] To investigate the insulation effects on
230 the charge transfer between the ferrocene unit and ITO electrode, the variation in the peak-to-peak
231 separation potentials (Fig. 4a; $\Delta E = E_p - E^{\circ\prime}$, where E_p is the peak potential and $E^{\circ\prime}$ is the formal
232 potential) with increasing scan rate was determined to construct the trumpet plots (Fig. 4b).[57,59,60] While the
233 peak-to-peak separation of uninsulated **4'** occurred at $\log(v) = 0.6$ ($v = 4$ V s^{-1}), insulated **4** did not display
234 any significant peak-to-peak separation, even at a high scan rate of $\log(v) = 2$ ($v = 100$ V s^{-1}). This indicated
235 that the rate of charge transfer between the ITO electrode and **4** increased, owing to the insulated structure.

In our previous study on the single molecular conductance of insulated molecules, the conductance of single insulated conjugation was lower than that of the corresponding uninsulated molecule. This occurred because the π-conjugated backbone was twisted, owing to insulation by PM α–CD.[61] In this study, however, the insulated structure improved the charge-transfer efficiency relative to the uninsulated counterpart, indicating that the insulation enhanced the charge transfer at the interface rather than on the π-conjugated core. The highly efficient charge transfer between **4** and the ITO electrode were attributed to the inhibition of π–π interaction and intermolecular charge transfer. Indeed, the intermolecular charge transfer between the bare π-conjugated cores of uninsulated **4'** decreased the charge-transfer efficiency. Thus, appropriate π-aggregation inhibition at the organic–inorganic interface utilizing [1]rotaxanes structures is a promising strategy for developing exceptional electrical devices, owing to the high charge-transfer efficiency.

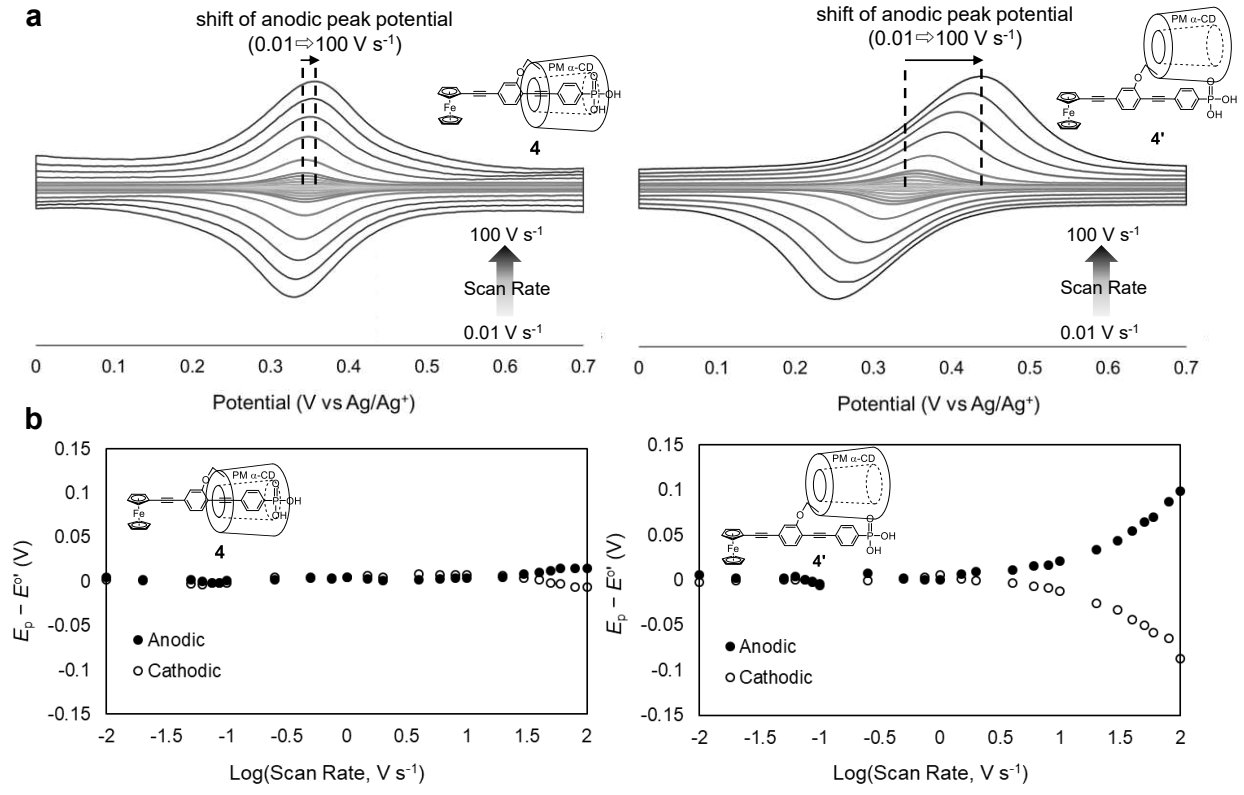

Fig. 4 Interfacial charge transfer. a Cyclic voltammograms of immobilized **4** and **4'** at various scan rates. **b** Trumpet plot for immobilized **4** and **4'**. Conditions: 0.1 M CH_2Cl_2 solution of $TBAPF_6$.

Surface Functionalization with Metalloporphyrin

The isolated surface π-conjugations were effectively applied to electrical devices based on organic–inorganic hybrid materials. To provide functionalities on the hybrid materials, we focused on the immobilization of metal complexes through metal–ligand coordination, which have been widely utilized for dyes and surface inorganic catalysis.[62,6362] In particular, the modification of metalloporphyrin analogs onto metal oxide surfaces have been effectively applied to artificial photosynthesis and electrosynthesis devices.[64,65] In the current study, the 4-pyridyl group was introduced as a coordination point into insulated and uninsulated structures to obtain **5** and **5'**, respectively (Scheme S4). To evaluate the potential of **5** for application to surface engineering, we first investigated the complexation behavior between **5** (or **5'**) and **Rh^{III}Cl(OEP)** (OEP: octaethylporphyrin), both in the solution system and on the surface system. In the former, the coordination between compound S12[66] and **Rh^{III}Cl(OEP)** was confirmed from the characteristic up-field shifts observed for complexation in the ^{1}H NMR spectra (Figs. S5 and S6). In addition, the complexation was applied to the surface modifications. Thus, the ITO substrate was immersed in a solution of **5** or **5'** in MeOH (1000 μM) overnight, and subsequently submerged in a solution of **Rh^{III}Cl(OEP)** in CH_2Cl_2 (200 μM) for 2 h to obtain **Rh^{III}Cl(OEP)**–**5**/ITO (Fig. 5a) or **Rh^{III}Cl(OEP)**–**5'**/ITO, respectively. In the AFM images of the modified substrates (Fig. S7), there were no distinct aggregation structures on the surface of **Rh^{III}Cl(OEP)**–**5**/ITO. In contrast, many large protrusions were observed as aggregation structures on its uninsulated counterpart. Surface modification of the Rh–porphyrin complex was confirmed by UV–vis absorption and XPS analysis. In the differential UV–vis absorbance spectrum of **Rh^{III}Cl(OEP)**–**5**/ITO (Fig. S8b, red line), the characteristic Soret and Q bands of porphyrin were observed. Conversely, no characteristic porphyrin absorption bands were observed following the direct immersion of the ITO substrate into the **Rh^{III}Cl(OEP)** solution without immersion into a solution of **5** (Fig. S8b, blue line). Moreover, the maximum absorption wavelength of **Rh^{III}Cl(OEP)**–**5**/ITO corresponded to that observed in the **Rh^{III}Cl(OEP)**–**S12** solution (Fig. 5b). The XPS survey spectra of **Rh^{III}Cl(OEP)**–**5**/ITO also showed Rh 3d peaks at 310 and 315 eV (Fig. 5c). These results strongly support

the formation of **Rh^{III}Cl(OEP)–5** complexes with ITO as the hybrid interface. According to the integral areas of the Rh $3d_{3/2}$ and P 2p peaks, which were normalized by that of the In 3d peak derived from the ITO substrate, the ratio of Rh-porphyrin-to-insulated **5** in **Rh^{III}Cl(OEP)–5**/ITO was 1:1 (Table S4). On the other hand, that between Rh-porphyrin and **5'** in **Rh^{III}Cl(OEP)–5'**/ITO was 1.7:1, because of the non-independence of the uninsulated molecule on the surface. According to the space filling model obtained by calculation (Fig. S10), the molecular size of **Rh^{III}Cl(OEP)** was near-identical to the diameter of PM α–CD. This permitted high-density packing of the metalloporphyrin portion, while simultaneously avoiding metalloporphyrin overlapping on the metal oxide surface. Thus, this sequentially coordinated modification utilizing insulated **5** allowed an easy approach for introducing a large metalloporphyrin of high crystallinity and low solubility onto the metal oxide surface via metal–ligand axial coordination. This was achieved without complicated synthesis of the metalloporphyrin, and bypassed aggregation structure formation on the metal oxide surface.

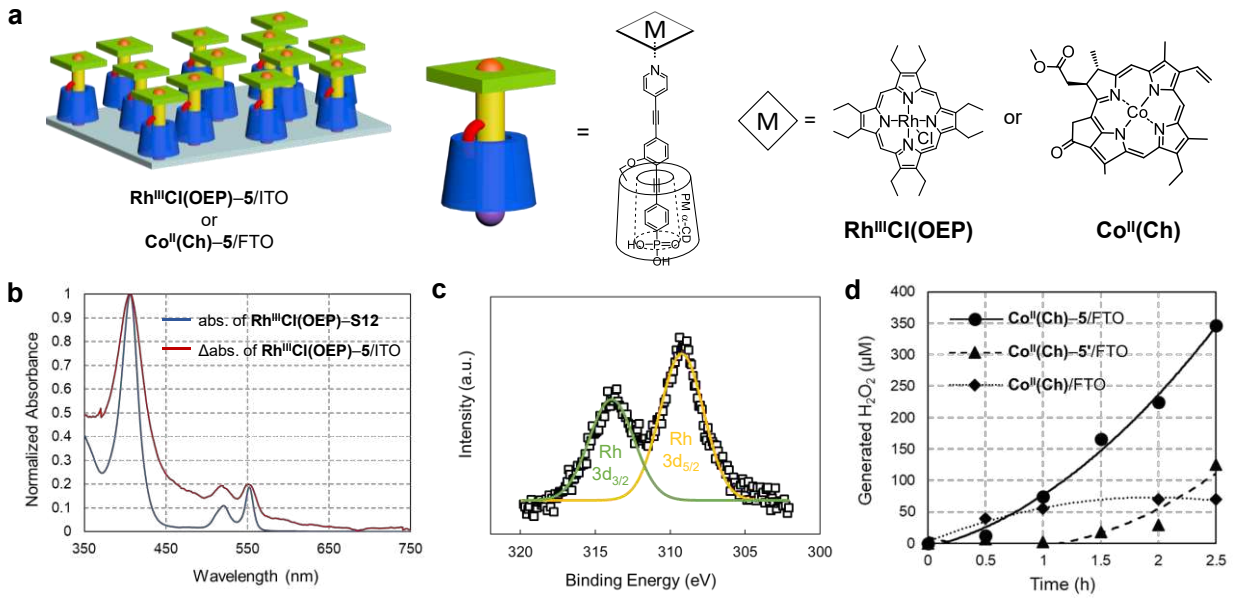

Fig. 5 Coordination of metalloporphyrin and its analog to insulated molecules. a Image of **Rh^{III}Cl(OEP)–5**/ITO and **Co^{II}(Ch)–5**/FTO. **b** Normalized UV–vis absorption spectra of the **Rh^{III}Cl(OEP)–5**/ITO and $CHCl_3$ solution of the **Rh^{III}Cl(OEP)–S12** (1×10^{-5} M) complex. **c** XPS spectra

of Rh $3d_{3/2}$ (green line) and Rh $3d_{5/2}$ (yellow line) for **Rh^{III}Cl(OEP)**–**5**/ITO substrate. **d** H_2O_2 production of **Co^{II}(Ch)**–**5**/FTO (solid line), **Co^{II}(Ch)**–**5'**/FTO (dashed line), and **Co^{II}(Ch)**/FTO (dotted line) as working electrodes. The reactions were carried out by applying constant voltage (E = 0.41 V vs. Ag/AgCl) in an O_2-saturated perchlorate buffer solution (pH 1.3, 100 mM, 11 mL).

Electrocatalysis for H_2O_2 generation

Surface engineering using insulated molecules and metalloporphyrin derivatives was next applied to the electrical devices. Cobalt chlorin complexes [**Co^{II}(Ch)**] have been reported as highly efficient and selective molecular catalysts for the two-electron selective reduction of dioxygen (O_2) to yield hydrogen peroxide (H_2O_2) in homogeneous solution.[67] However, the selectivity decreases when the catalysts are immobilized on the electrode surface. Owing to the disordered morphology of the surface-adsorbed **Co^{II}(Ch)**, a μ-1,2-peroxo dinuclear structure[68] is formed, which carries on the four-electron-reduced dioxygen, producing H_2O as a by-product.[69] In this study, the high-degree independency and outstanding electrical properties of a [1]rotaxane-based hybrid system were applied to the **Co^{II}(Ch)**-catalyzed electrochemical device, to prevent the formation of μ-1,2-peroxo dinuclear structures and enhance the charge-transfer efficiency. Insulated **5** and uninsulated **5'** coordinated to **Co^{II}(Ch)** were immobilized on FTO to form **Co^{II}(Ch)**–**5**/FTO[70] (Fig. 5a) and **Co^{II}(Ch)**–**5'**/FTO electrodes through the Langmuir–Blodgett (LB) technique at the same surface pressure, respectively. Both metal complexes formed a solid condensed monolayer on the FTO surface according to the pressure–area (π–A) isotherms (Fig. S12). In addition, the Soret and Q bands of **Co^{II}(Ch)** were observed in the differential absorption spectra of modified FTO in both **Co^{II}(Ch)**–**5**/FTO and **Co^{II}(Ch)**–**5'**/FTO (Fig. S13).

During the electrocatalytic synthesis, the **Co^{II}(Ch)**–**5**/FTO system showed the best H_2O_2 production efficiency (Fig. 5d). In contrast, the **Co^{II}(Ch)**/FTO system, which directly deposited the catalyst on the FTO surface by the LB technique, exhibited the lowest production efficiency. The H_2O_2 production of the **Co^{II}(Ch)**/FTO system declined after 1 h because of catalyst desorption, owing to the structure without

phosphonic acid-based-anchoring portion. In addition, the catalyst films formed a μ-1,2-peroxo dinuclear structure on the surface which, as previously mentioned, yielded H_2O as a byproduct, thereby decreasing the selectivity. Unlike the **Co^{II}(Ch)**/FTO system, the **Co^{II}(Ch)–5'**/FTO system contained an anchoring portion to improve the adsorption stability. Although **Co^{II}(Ch)–5'**/FTO exhibited a similar adsorption density to that of its insulated counterpart in line with the absorption spectra (Fig. S14), the performance of the **Co^{II}(Ch)–5'**/FTO system was inferior. According to the previously described charge-transfer experiment, the uninsulated structure of **5'** was detrimental to charge transfer. This was suggested to be one of the reasons for the lower production efficiency compared to that of the **Co^{II}(Ch)–5**/FTO system. In addition, because of the dependence on the uninsulated structure, the uninsulated **Co^{II}(Ch)–5'** complex formed a monolayer with intrinsically loose alignment on the FTO surface, while part of the **Co^{II}(Ch)** portion formed a μ-1,2-peroxo dinuclear structure, decreasing the selectivity. Consequently, improvement in the production efficiency of the **Co^{II}(Ch)–5**/FTO system should be considered independently of the insulated surface structure and charge transfer improvement.

Discussion

In summary, [1]rotaxane molecules bearing a phosphonic acid-derived PE as the conjugated backbone and PM α–CD as a protective macrocycle were immobilized on metal oxide surfaces via a wet process. AFM and CV analyses revealed the insulation effects on the hybrid system of the [1]rotaxanes. The insulated molecules were immobilized on the metal oxide surfaces in ideal state without aggregation and displayed high charge-transfer efficiency at the interface, as compared to their uninsulated counterparts. The high advantages of insulation were applied to electrocatalysis as electrical hybrid devices. The [1]rotaxane system was utilized for the platform to introduce organic functionalities on the inorganic electrode. The catalytic efficiency of the cobalt chlorin complex was markedly improved by utilizing insulated molecules. These results indicate the importance of the [1]rotaxane strategy in isolating molecules from unfavorable molecular interactions, even at the hybrid interface, providing excellent performance in electrical hybrid devices. This methodology possesses high potential to upgrade the performances of

existing electrical devices based on π-conjugated hybrid systems to outstanding devices, by improving the independency and charge-transfer efficiency of the π-conjugated molecules at the hybrid interface. The [1]rotaxane strategy can be considered as a general and versatile method for interfacial control, even for other types of hybrid junctions in addition to phosphonic acid and tin oxides, which would efficiently solve the conventional problems observed in hybrid interfaces composed of π-conjugated molecules and inorganic materials.

Methods

Synthesis of **1**

1,4-diiodobenzene (2.4 g, 7.27 mmol) was dissolved in degassed $^{i}Pr_2NH$/THF (6/3 mL). Under an argon, **S1**(1.00 g, 737 μmol), $PdCl_2(PPh_3)_2$ (51.8 mg, 73.8 μmol) and CuI (7.0 mg, 36.8 μmol) were added to the solution. The reaction mixture was stirred under an argon at room temperature overnight. The solvent was removed *in vacuo*, and the residue was purified by column chromatography on silica gel (1:1 toluene:EtOAc and 85:15 EtOAc:MeOH) to yield **S2** as an orange solid (845 mg, 542 μmol, 74%).

Under an argon atmosphere, $Pd(OAc)_2$ (11.6 mg, 51.6 μmol), dppf (57.3 mg, 103 μmol) and KOAc (50.6 mg, 516 μmol) were placed in the reaction vessel. THF (20 mL) was introduced and the mixture was stirred and heated at 68 °C. After 5 min, **S2** (805 mg, 517 μmol), diethyl phosphite (666 μL, 5.16 mmol) and triethylamine (TEA) (357 μL, 2.58 μmol) were added to the mixture. The reaction mixture was stirred at 68 °C overnight. The mixture was dried *in vacuo*, and the residue was purified by GPC with $CHCl_3$ as the eluent to yield **1** as an orange solid (609 mg, 388 μmol, 72%). *ESI MS*: (*m/z*) 1568.665 ($[M+H]^+$, $C_{71}H_{111}NO_{35}P$, calcd. 1568.667). *^{1}H NMR (500 MHz, $CDCl_3$, r.t.)*, δ: 7.82−7.80 (m, 4H, ArH), 7.71−7.69 (m, 2H, ArH), 7.61 (d, J = 8.5 Hz, 1H, ArH), 5.09−2.99 (m, 97H, CD−H, OCH_3, OCH_2CH_3), 1.32 (t, J = 6.3 Hz, 6H, OCH_2CH_3). *^{13}C NMR (126 MHz, $CDCl_3$, r.t.)*, δ: 159.55, 148.20, 133.46, 131.82 (d, J = 7.4 Hz), 131.72 (d, J = 12.6 Hz), 129.08 (d, J = 189.8 Hz), 126.50, 126.47, 119.4, 116.0, 106.7, 100.44, 100.29,

100.21, 100.18, 100.13, 100.03, 97.3, 86.8, 82.73, 82.60, 82.54, 82.52, 82.47, 82.21, 82.19, 82.15 (peaks overlapped), 81.98, 81.94, 81.18, 81.14 (peaks overlapped), 81.12, 80.95, 71.71, 71.54 (peaks overlapped), 71.51, 71.44, 71.32, 71.29 (peaks overlapped), 71.28, 71.20, 70.19, 68.3, 62.33, 62.28, 61.88, 61.85 (peaks overlapped), 61.81, 61.79 (peaks overlapped), 59.33, 59.11 (peaks overlapped), 58.89, 58.25, 57.91, 57.86, 57.82, 57.81, 57.30, 16.33 (d, J = 6.5 Hz). *^{31}P NMR (202 MHz, $CDCl_3$, r.t.)*, δ: 17.59.

Synthesis of **2**

1 (30 mg, 19 μmol) was added into MeOH/H_2O (1/1, 30 mL), and the solution was stirred at 60 °C overnight. The reaction mixture was evaporated to reduce MeOH. The mixture was diluted with $CHCl_3$ and washed with water. The organic layer was separated and dried over $MgSO_4$, and then filtered. The solvent was removed by evaporation to yield **2** as a pale yellow solid (27 mg, 17 μmol, 89%) without further purification. *ESI MS*: (*m/z*) 1590.648 ($[M+Na]^+$, $C_{71}H_{110}NO_{35}PNa$, calcd. 1590.649). *^{1}H NMR (500 MHz, $CDCl_3$, r.t.)*, δ: 8.23−8.22 (m, 2H, ArH), 8.00−7.98 (m, 4H, ArH), 7.80 (d, J = 7.9 Hz, 1H, ArH), 5.06−2.99 (m, 97H, CD−H, OCH_3, OCH_2CH_3), 1.26 (dd, J = 11.3, 6.7 Hz, 6H, OCH_2CH_3). *^{13}C NMR (126 MHz, $CDCl_3$, r.t.)*, δ: 162.06, 148.17, 134.05, 132.32 (d, J = 13.9 Hz), 131.41 (d, J = 10.1 Hz), 130.35 (d, J = 191.5 Hz), 125.19, 123.28, 117.90, 116.81, 100.72, 100.54, 100.11, 99.98, 99.90, 97.96, 97.19, 87.39, 83.56, 83.26, 82.90, 82.54, 82.37, 82.34, 82.28 (peaks overlapped), 82.02 (peaks overlapped), 81.93, 81.91, 81.65, 81.34, 81.15, 81.09, 81.03, 80.98, 72.03 (peaks overlapped), 71.92, 71.57, 71.48, 71.44, 71.33 (peaks overlapped), 71.26, 71.12, 70.62, 70.48, 61.96, 61.93, 61.84, 61.79, 61.71, 61.66, 61.58, 61.56, 58.99, 58.88, 58.81, 58.57, 58.51, 58.30, 58.01, 57.70, 57.62, 57.54, 57.46, 16.12 (d, J = 6.3 Hz). *^{31}P NMR (202 MHz, $CDCl_3$, r.t.)*, δ: 16.46.

Synthesis of **3'**

Under a nitrogen, **1** (30.5 mg, 19.4 μmol) was dissolved in TEA/CH_2Cl_2 (0.16/2 mL), and TMSBr (49 μL, 383 μmol) was added into the solution. After the reaction mixture was stirred at room temperature for 12 h, the solvent was removed by vacuum distillation and 5 mL of methanol was added to the resulting crude.

After the dissolved crude was stirred at room temperature for another 12 h, the solvent was evaporated *in vacuo*. The residue was dissolved in $CHCl_3$ and washed by dilute aqueous HCl solution. The organic layer was separated and dried over $MgSO_4$, then the solvent was removed *in vacuo*. Furthermore, the residue was dissolved in MeOH and washed by hexane. The MeOH layer was collected and concentrated to yield **3'** as a pale yellow solid (28.0 mg, 18.5 μmol, 95%). Surface immobilizations were carried out without further purifications. *ESI MS*: (*m/z*) 1510.591 ($[M–H]^-$, $C_{67}H_{101}NO_{35}P$, calcd. 1510.590). *^{1}H NMR (500 MHz, $CDCl_3$, r.t.)*, δ: 7.83−7.77 (m, 4H, ArH), 7.66−7.62 (broad, 2H, ArH), 7.56 (d, *J* = 8.1 Hz, 1H, ArH), 5.07−2.97 (m, 93H, CD−H, OCH_3). *^{13}C NMR (126 MHz, $CDCl_3$, r.t.)*, δ: 159.54, 148.10, 133.21, 131.50 (d, *J* = 16.4 Hz), 131.00 (d, *J* = 10.1 Hz), 125.98, 119.43, 115.90, 106.93, 100.29 (peaks overlapped), 100.17 (peaks overlapped), 100.09 (peaks overlapped), 99.98 (peaks overlapped), 97.48, 86.53, 82.63, 82.55, 82.46 (peaks overlapped), 82.38, 82.16 (peaks overlapped), 82.10 (peaks overlapped), 82.02, 81.96, 81.76, 81.25, 81.17 (peaks overlapped), 81.11, 71.69, 71.66, 71.49 (peaks overlapped), 71.28 (peaks overlapped), 71.23, 71.17, 70.34, 68.30, 67.94, 61.86, 61.79 (peaks overlapped), 61.74 (peaks overlapped), 61.72, 59.30, 59.09, 59.08, 59.06, 58.87, 58.16, 57.87, 57.81 (peaks overlapped), 57.77, 57.34. *^{31}P NMR (202 MHz, $CDCl_3$, r.t.)*, δ: 18.74.

Synthesis of **3**

Under a nitrogen, **2** (27.6 mg, 17.6 μmol) was dissolved in TEA/CH_2Cl_2 (0.15/2 mL), and TMSBr (45 μL, 383 μmol) was added into the solution, and the reaction mixture was stirred at room temperature for 12 h. After the solvent was removed by vacuum distillation, 5 mL of methanol was added to the resulting crude and stirred at room temperature for another 12 h. Then, the solvent was evaporated by vacuum. After the residue was dissolved in $CHCl_3$ and washed by dilute aqueous HCl solution, the organic layer was separated and dried over $MgSO_4$ and the solvent was removed *in vacuo*. Furthermore, the residue was dissolved in MeOH and washed by hexane. The MeOH layer was separated and concentrated to yield **3** as a pale yellow solid (16.4 mg, 10.8 μmol, 61%). Surface immobilizations were carried out without further purifications. *ESI MS*: (*m/z*) 1510.593 ($[M–H]^-$, $C_{67}H_{101}NO_{35}P$, calcd. 1510.590). *^{1}H NMR (500 MHz, $CDCl_3$, r.t.)*, δ: 8.22

(d, J = 5.0 Hz, 2H, ArH), 8.08−8.03 (m, 4H, ArH), 7.81 (d, J = 8.2 Hz, 1H, ArH), 5.09−3.01 (m, 93H, CD−H, OCH_3). *^{13}C NMR (126 MHz, $CDCl_3$, r.t.)*, δ: 162.11, 148.16, 133.92, 132.14 (d, J = 13.9 Hz), 131.07 (d, J = 10.1 Hz), 123.61, 118.06, 116.98, 100.64, 100.23, 100.08, 100.06, 99.92, 97.93, 83.54, 83.08, 82.56, 82.45, 82.32, 82.12, 82.07, 81.96, 81.77, 81.55, 81.34, 81.17, 81.15, 81.08, 80.93, 80.72, 80.55, 80.46, 72.24, 72.15, 71.68, 71.54 (peaks overlapped), 71.30, 71.28, 70.63, 61.82, 61.80, 61.64, 61.60, 61.55, 61.30, 59.12, 59.01, 58.91, 58.70, 58.65, 58.26, 57.90, 57.77, 57.72 (peaks overlapped), 57.68. *^{31}P NMR (202 MHz, $CDCl_3$, r.t.)*, δ: 16.86.

Synthesis of **4'**

Under a nitrogen, **S8** (29.8 mg, 17.2 μmol) was dissolved in TEA/CH_2Cl_2 (0.15/2 mL), and TMSBr (44 μL, 346 μmol) was added into the solution. The reaction mixture was stirred at room temperature for 12 h. After this reaction completed, the solvent was removed by vacuum distillation and 5 mL of methanol was added to the resulting crude. After the dissolved crude was stirred at room temperature for another 12 h, the solvent was evaporated by vacuum. The residue was dissolved in $CHCl_3$ and washed by dilute aqueous HCl solution. The organic layer was separated and dried over $MgSO_4$, then the solvent was removed *in vacuo*. Furthermore, the residue was dissolved in MeOH and washed by hexane. The MeOH layer was separated and concentrated to yield **4'** as a red solid (26.5 mg, 15.8 μmol, 92%). Surface immobilizations were carried out without further purifications. *HR–ESI MS*: (*m/z*) 1673.6056 ($[M–H]^–$, $C_{79}H_{110}FeO_{33}P$, calcd. 1673.6016). *^{1}H NMR (500 MHz, $CDCl_3$, r.t.)*, δ: 7.86 (dd, J = 11.6, 8.1 Hz, 2H, ArH), 7.56 (d, J = 5.9 Hz, 2H, ArH), 7.43 (d, J = 7.6 Hz, 1H, ArH), 7.07−7.04 (m, 2H, ArH), 5.22−3.03 (m, 102H, CD−H, OCH_3, FcH). *^{13}C NMR (126 MHz, $CDCl_3$, r.t.)*, δ: 158.80, 133.22, 130.80 (d, J = 10.1 Hz), 130.71 (d, J = 13.9 Hz), 124.61, 124.09, 123.93, 114.58, 112.78, 100.62, 100.25, 100.18, 100.16, 100.13, 99.73, 95.40, 90.06, 86.54, 85.92, 82.87, 82.51 (peaks overlapped), 82.46, 82.21, 82.16 (peaks overlapped), 81.91, 81.70, 81.26, 81.20 (peaks overlapped), 81.15 (peaks overlapped), 80.96, 71.94, 71.78, 71.52 (peaks overlapped), 71.47 (peaks overlapped), 71.33 (peaks overlapped), 71.29 (peaks overlapped), 71.21, 70.58, 69.94, 69.00, 67.63, 64.92,

61.88 (peaks overlapped), 61.83 (peaks overlapped), 61.77, 61.71, 59.33, 59.20, 59.11 (peaks overlapped), 59.09, 58.35, 57.91, 57.81 (peaks overlapped), 57.78, 57.33. *^{31}P NMR (202 MHz, $CDCl_3$, r.t.)*, δ: 12.55.

Synthesis of **4**

Under a nitrogen, **S6** (34.6 mg, 20 μmol) was dissolved in TEA/CH_2Cl_2 (0.17/2 mL), and TMSBr (77 μL, 606 μmol) was added into the solution. The reaction mixture was stirred at room temperature for 12 h. After this reaction completed, the solvent was removed by vacuum distillation and 5 mL of methanol was added to the resulting crude. After the dissolved crude was stirred at room temperature for another 12 h, the solvent was evaporated by vacuum. The residue was dissolved in $CHCl_3$ and washed by dilute aqueous HCl solution. The organic layer was separated and dried over $MgSO_4$, then the solvent was removed *in vacuo*. Furthermore, the residue was dissolved in MeOH and washed by hexane. The MeOH layer was separated and concentrated to yield **4** as a red solid (28.5 mg, 17 μmol, 85%). Surface immobilizations were carried out without further purifications. *HR–ESI MS*: (*m/z*) 1673.6048 ([M–H]$^-$, $C_{79}H_{110}FeO_{33}P$, calcd. 1673.6016). *^{1}H NMR (500 MHz, $CDCl_3$, r.t.)*, δ: 8.15 (broad, 2H, ArH), 7.99 (dd, *J* = 13.2, 8.1 Hz, 2H, ArH), 7.43 (d, *J* = 7.8 Hz, 1H, ArH), 7.25 (d, *J* = 8.5 Hz, 2H, ArH), 5.07−2.85 (m, 102H, CD−H, OCH_3, Fc−H). *^{13}C NMR (126 MHz, $CDCl_3$, r.t.)*, δ: 161.83, 132.98, 131.90 (d, *J* = 15.1 Hz), 131.05 (d, *J* = 10.1 Hz), 126.24, 126.14, 124.71, 115.76, 100.67, 100.13, 100.06, 99.98, 99.90, 97.93, 94.41, 91.90, 88.88, 84.72, 83.82, 82.70, 82.55, 82.44, 82.29, 82.10, 82.04, 81.89, 81.75, 81.68, 81.54, 81.28, 81.15, 81.09, 80.86, 80.64, 80.49, 72.47, 72.06, 71.80, 71.55 (peaks overlapped), 71.48, 71.45, 71.33, 71.17, 71.12, 70.60, 70.56, 70.21, 70.02, 69.28, 64.25, 61.86, 61.82, 61.74, 61.60, 61.30, 61.26, 59.13, 59.09, 58.94, 58.80, 58.76, 58.19, 57.89, 57.82, 57.73 (peaks overlapped), 57.69. *^{31}P NMR (202 MHz, $CDCl_3$, r.t.)*, δ: 17.47.

Synthesis of **5'**

Under a nitrogen, **S13** (27.7 mg, 17.0 μmol) was dissolved in TEA/CH_2Cl_2 (0.23/2.5 mL), and TMSBr (71 μL, 554 μmol) was added into the solution. The reaction mixture was stirred at room temperature for 12 h. After this reaction completed, the solvent was removed by vacuum distillation and 5 mL of methanol was

added to the resulting crude. After the dissolved crude was stirred at room temperature for another 12 h, the solvent was evaporated by vacuum. The residue was dissolved in $CHCl_3$ and washed by dilute aqueous HCl solution. The organic layer was separated and dried over $MgSO_4$, then the solvent was removed *in vacuo*. Furthermore, the residue was dissolved in MeOH and washed by hexane. The MeOH layer was separated and concentrated to yield **5'** as a yellow solid (26.3 mg, 16.8 μmol, 99%). Surface immobilizations were carried out without further purifications. *HR–ESI MS*: (*m/z*) 1566.6326 ($[M–H]^-$, $C_{74}H_{105}NO_{33}P$, calcd. 1566.6306). *^{1}H NMR (500 MHz, MeOD, r.t.)*, δ: 8.64 (broad, 2H, PyH), 7.84−7.80 (m, 2H, ArH), 7.75−7.73 (m, 2H, ArH), 7.67 (d, J = 4.0 Hz, 2H, PyH), 7.52 (d, J = 7.8 Hz, 1H, ArH), 7.27 (s, 1H, ArH), 7.23 (d, J = 7.9 Hz, 1H, ArH), 5.13−2.97 (m, 93H, CD−H, OCH_3). *^{13}C NMR (126 MHz, MeOD, r.t.)*, δ: 172.96, 160.70, 148.63, 135.59, 134.26, 132.53 (d, J = 13.9), 132.09 (d, J = 10.1 Hz), 127.83, 126.62 (d, J = 191.5 Hz), 124.09, 116.81, 115.61, 101.38, 100.93, 100.89, 100.45, 100.33, 100.28, 100.22, 97.21, 96.17, 88.45, 83.73, 83.46, 83.40, 83.36, 83.33, 83.26, 83.08 (peaks overlapped), 83.02, 82.97, 82.87, 82.80 (peaks overlapped), 82.69, 73.35, 73.32, 73.23, 73.20, 72.98, 72.91, 72.60, 72.54, 72.45, 72.37, 71.74, 69.26, 62.31, 62.28, 62.15, 62.12, 62.04, 62.01, 59.57, 59.42, 59.35 (peaks overlapped), 59.32, 59.10, 58.66, 58.53, 58.44, 58.43, 58.08, 49.00. *^{31}P NMR (202 MHz, MeOD, r.t.)*, δ: 14.60.

Preparation of Modified ITO Substrates

ITO substrates (surface roughness: average 0.7 nm (KURAMOTO)) or single crystalline ITO substrates (atomically flat terraces and steps (<0.2 nm))[60,61] was used. Spectroscopic grade MeOH and $CHCl_3$ were used as solvents. Prior to use, the ITO surface was annealed with ozone at 200 °C for 15 min. An annealed ITO substrate was immersed in a methanol solution of the molecules for 12 h at room temperature, followed by rinsing in MeOH as well as chloroform and drying through nitrogen flow.

Electrochemical Measurement

Cyclic voltammetry (CV) measurements were taken using a CHI 600B potentiostat with a one-compartment cell under air. All measurements were carried out in 0.1 M of tetrabutylammonium hexafluorophosphate

(TBAPF$_6$) in CH_2Cl_2. The **4**−modified ITO substrate and **4'**−modified ITO substrate were used as the working electrode (electrode area: 3.5^2 π mm^2), and a platinum wire was used as the counter electrode. Potentials are referenced to an Ag/Ag^+ (10 mM $AgNO_3$ in 0.1 M $TBAClO_4$−MeCN) electrode.

Electrochemical hydrogen peroxide (H_2O_2) production

Electrochemical H_2O_2 production was performed using a conventional three-electrode cell using **Co^{II}(Ch)**−**5**/FTO or **Co^{II}(Ch)**−**5'**/FTO, an Au coil counter electrode and a Ag/AgCl reference electrode in an oxygen (O_2)−saturated aqueous solution (8 mL) in an aqueous perchloric acid (pH 1.3, 0.1 M, 11.0 mL) by applying constant voltage (E = 0.41 V vs. Ag/AgCl) to a working electrode. The cell was kept in dark to prevent the unexpected decomposition of produced H_2O_2. The O_2 bubbling was continued during the photocatalytic reaction. The concentration of H_2O_2 produced in the reaction solution was determined by spectroscopic titration with an acidic solution of oxo[5,10,15,20-tetra(4-pyridyl)porphyrinato]titanium(IV) complex (Ti(TPyP)). The stock solution of Ti(TPyP) was prepared by dissolving 3.40 mg of Ti(TPyP) in 100 mL of 50 mM hydrochloric acid. An aliquot of the reaction solution was sampled and diluted with a certain amount of water depending on the concentration of H_2O_2. The diluted H_2O_2 solution was mixed to 0.25 mL of 4.8 M an aqueous solution of $HClO_4$ (4.8 M, 0.25 mL) and the stock solution of Ti(TPyP) (0.25 mL). The mixed solution was then allowed to stand for 5 min at room temperature. The sample solution was diluted to 2.5 mL with water and used for the UV−Vis absorption analysis to determine the absorbance at λ = 450 nm. A blank solution was prepared in a similar manner by adding distilled water instead of the sample solution to Ti(TPyP) in the same volume with its absorbance designated as A_B. The difference in absorbance was determined as follows: $\Delta A_{450} = A_S - A_B$. The amount of H_2O_2 produced was determined based on ΔA_{450} and the volume of the solution.

Data Availability

All other data that support the findings of this study are available within the article and its Supplementary Information, or from the corresponding author upon reasonable request.

References

1. Mir, S. H.; Nagahara, L. A.; Thundat, T.; Mokarian-Tabari, P.; Furukawa, H.; Khosla, A. Review—organic–inorganic hybrid functional materials: an integrated platform for applied technologies. *Journal of The Electrochemical Society* **165**, B3137–B3156 (2018).

2. Mallakpour, S.; Madani, M. A review of current coupling agents for modification of metal oxide nanoparticles. *Prog. Org. Coatings* **86**, 194–207 (2015).

3. Minamiki, T.; Ichikawa, Y.; Kurita, R. The power of assemblies at interfaces: nanosensor platforms based on synthetic receptor membranes. *Sensors* **20**, 2228–2255 (2020).

4. Zahran, Z. N.; Tsubonouchi, Y.; Mohamed, E. A.; Yagi, M. Recent advances in the development of molecular catalyst-based anodes for water oxidation toward artificial photosynthesis. *ChemSusChem* **12**, 1775–1793 (2019).

5. Simão, C.; Mas-Torrent, M.; Crivillers, N.; Lloveras, V.; Artés, J. M.; Gorostiza, P.; Veciana, J.; Rovira, C. A robust molecular platform for non-volatile memory devices with optical and magnetic responses. *Nat. Chem.* **3**, 359–364 (2011).

6. Wei, C.; Zhuang, J.; Zhang, D.; Guo, W.; Yang, D.; Xie, Z.; Tang, J.; Su, W.; Zeng, H.; Cui, Z. Pyridine-based electron-transport materials with high solubility, excellent film-forming ability, and wettability for inkjet-printed OLEDs. *ACS Appl. Mater. Interfaces* **9**, 38716–38727 (2017).

7. Huang, Y.; Kramer, E. J.; Heeger, A. J.; Bazan, G. C. Bulk heterojunction solar cells: morphology and performance relationships. *Chem. Rev.* **114**, 7006–7043 (2014).

8. Liu, D.; Miao, Q. Recent progress in interface engineering of organic thin film transistors with self-assembled monolayers. *Mater. Chem. Front.* **2**, 11–21 (2018).

9. Pujari, S. P.; Scheres, L.; Marcelis, A. T. M.; Zuilhof, H. Covalent surface modification of oxide surfaces. *Angew. Chem. Int. Ed.* **53**, 6322–6356 (2014).

10. Miyachi, M.; Kobayashi, T.; Nishihara, H.; Yamanoi, Y.; Sendo, J.; Maeda, H.; Sakamoto, R.; Yabusaki, Y. A new method to generate arene-terminated Si(111) and Ge(111) surfaces via a palladium-catalyzed arylation reaction. *J. Am. Chem. Soc.* **134**, 20433–20439 (2012).

11. Chouirfa, H.; Bouloussa, H.; Migonney, V.; Falentin-Daudré, C. Review of titanium surface modification techniques and coatings for antibacterial applications. *Acta Biomater.* **83**, 37–54 (2019).

12. Meng, X. An overview of molecular layer deposition for organic and organic–inorganic hybrid materials: mechanisms, growth characteristics, and promising applications. *J. Mater. Chem. A* **5**, 18326–18378 (2017).

13. Zhang, L.; Cole, J. M. Dye aggregation in dye-sensitized solar cells. *J. Mater. Chem. A* **5**, 19541–19559 (2017).

14. Feng, S.; Li, Q. S.; Sun, P. P.; Niehaus, T. A.; Li, Z. S. Dynamic characteristics of aggregation effects of organic dyes in dye-sensitized solar cells. *ACS Appl. Mater. Interfaces* **7**, 22504–22514 (2015).

15. Feng, S.; Li, Q. S.; Yang, L. N.; Sun, Z. Z.; Niehaus, T. A.; Li, Z. S. Insights into aggregation effects on optical property and electronic coupling of organic dyes in dye sensitized solar cells. *J. Power Sources* **273**, 282–289 (2015).

16. Kong, G. D.; Byeon, S. E.; Park, S.; Song, H.; Kim, S. Y.; Yoon, H. J. Mixed molecular electronics: tunneling behaviors and applications of mixed self-assembled monolayers. *Adv. Electron. Mater.* **6**, 1901157 (2020).

17. Magomedov, A.; Al-Ashouri, A.; Kasparavičius, E.; Strazdaite, S.; Niaura, G.; Jošt, M.; Malinauskas, T.; Albrecht, S.; Getautis, V. Self-assembled hole transporting monolayer for highly efficient perovskite solar cells. *Adv. Energy Mater.* **8**, 1801892 (2018).

18. Bumm, L. A.; Arnold, J. J.; Cygan, M. T.; Dunbar, T. D.; Burgin, T. P.; Jones, L.; Allara, D. L.; Tour, J. M.; Weiss, P. S. Are single molecular wires conducting? *Science* **271**, 1705–1707 (1996).

19. Tian, L.; Wang, Y.; Zhang, Y.; Li, X.; Wu, W.; Liu, B. Molecular engineering of indoline dyes and their application in dye-sensitized solar cells: effect of planarity and side chain on interfacial charge-transfer processes. *ACS Appl. Energy Mater.* **4**, 242–248 (2021).

20. Chen, H.; Lyu, G.; Yue, Y.; Wang, T.; Li, D. P.; Shi, H.; Xing, J.; Shao, J.; Zhang, R.; Liu, J. Improving the photovoltaic performance by employing alkyl chains perpendicular to the π-conjugated plane of an organic dye in dye-sensitized solar cells. *J. Mater. Chem. C* **7**, 7249–7258 (2019).

21. Royakkers, J.; Bronstein, H. Macrocyclic encapsulated conjugated polymers. *Macromolecules* **54**, 1083–1094 (2021).

22. Méhes, G.; Pan, C.; Bencheikh, F.; Zhao, L.; Sugiyasu, K.; Takeuchi, M.; Ribierre, J. C.; Adachi, C. Enhanced electroluminescence from a thiophene-based insulated molecular wire. *ACS Macro Lett.* **5**, 781–785 (2016).

23. Wang, J. C.; Hill, S. P.; Dilbeck, T.; Ogunsolu, O. O.; Banerjee, T.; Hanson, K. Multimolecular assemblies on high surface area metal oxides and their role in interfacial energy and electron transfer. *Chem. Soc. Rev.* **47**, 104–148 (2018).

24. Freitag, M.; Galoppini, E. Molecular host-guest complexes: shielding of guests on semiconductor surfaces. *Energy Environ. Sci.* **4**, 2482–2494 (2011).

25. Domi, Y.; Ikeura, K.; Okamura, K.; Shimazu, K.; Porter, M. D. Strong inclusion of inorganic anions into β-cyclodextrin immobilized to gold electrode. *Langmuir* **27**, 10580–10586 (2011).

26. Domi, Y.; Yoshinaga, Y.; Shimazu, K.; Porter, M. D. Characterization and optimization of mixed thiol-derivatized β-cyclodextrin/pentanethiol monolayers with high-density guest-accessible cavities. *Langmuir* **25**, 8094–8100 (2009).

27. Xue, M.; Yang, Y.; Chi, X.; Yan, X.; Huang, F. Development of pseudorotaxanes and rotaxanes: from synthesis to stimuli-responsive motions to applications. *Chem. Rev.* **115**, 7398–7501 (2015).

28. Sévery, L., Szczerbiński, J., Taskin, M. *et al.* Immobilization of molecular catalysts on electrode surfaces using host–guest interactions. *Nat. Chem.* (2021). https://doi.org/10.1038/s41557-021-00652-y

29. Choi, H.; Kang, S. O.; Ko, J.; Gao, G.; Kang, H. S.; Kang, M.-S.; Nazeeruddin, M. K.; Grätzel, M. An efficient dye-sensitized solar cell with an organic sensitizer encapsulated in a cyclodextrin cavity. *Angew. Chem., Int. Ed.* **48**, 5938–5941 (2009).

30. Ou, Y.; Chen, G.; Yin, J.; Yu, G. A.; Liu, S. H. Rotaxane based on terpyridyl bimetal ruthenium complexes and β-cyclodextrin as organic sensitizer for dye-sensitized solar cells. *J. Coord. Chem.* **64**, 3062–3067 (2011).

31. Rotaxane structures, where the bulky stopper units prohibit the dissociation between the axles and cyclic molecules, have not been relatively utilized as hybrid components to improve the charge-transfer efficiency at the interface. On the other hand, rotaxane structures on hybrid surfaces have been reported in memory and switch applications because their cyclic components undergo shuttling along the axle upon external stimulation; see (a) Baroncini, M.; Casimiro, L.; de Vet, C.; Groppi, J.; Silvi, S.; Credi, A. Making and operating molecular machines: a multidisciplinary challenge. *ChemistryOpen* **7**, 169–179 (2018). (b) Qu, D. H.; Wang, Q. C.; Zhang, Q. W.; Ma, X.; Tian, H. Photoresponsive host-guest functional systems. *Chem. Rev.* **115**, 7543–7588 (2015). (c) Jia, C.; Li, H.; Jiang, J.; Wang, J.; Chen, H.; Cao, D.; Stoddart, J. F.; Guo, X. Interface-engineered bistable [2]rotaxane-graphene hybrids with logic capabilities. *Adv. Mater.* **25**, 6752–6759 (2013). (d) Green, J. E.; Wook Choi, J.; Boukai, A.; Bunimovich, Y.; Johnston-Halperin, E.; Deionno, E.; Luo, Y.; Sheriff, B. A.; Xu, K.; Shik Shin, Y.; Tseng, H.-R.; Stoddart, J. F.; Heath, J. R. A 160-kilobit molecular electronic memory patterned at 1011 bits per square centimetre. *Nature* **445**, 414–417 (2007).

32. Leventis, A.; Royakkers, J.; Rapidis, A. G.; Goodeal, N.; Corpinot, M. K.; Frost, J. M.; Bučar, D. K.; Blunt, M. O.; Cacialli, F.; Bronstein, H. Highly luminescent encapsulated narrow bandgap polymers based on diketopyrrolopyrrole. *J. Am. Chem. Soc.*, **140**, 1622–1626 (2018).

603 33. Pan, C.; Zhao, C.; Takeuchi, M.; Sugiyasu, K. Conjugated oligomers and polymers sheathed with
604 designer side chains. *Chem. - An Asian J.* **10**, 1820–1835 (2015).

605 34. Terao, J.; Tsuda, S.; Tanaka, Y.; Okoshi, K.; Fujihara, T.; Tsuji, Y.; Kambe, N. Synthesis of organic-
606 soluble conjugated polyrotaxanes by polymerization of linked rotaxanes. *J. Am. Chem. Soc.* **131**,
607 16004–16005 (2009).

608 35. Liu, J.; Numata, Y.; Qin, C.; Islam, A.; Yang, X.; Han, L. Circle chain embracing donor-acceptor
609 organic dye: simultaneous improvement of photocurrent and photovoltage for dye-sensitized solar
610 cells. *Chem. Commun.* **49**, 7587–7589 (2013).

611 36. Terao, J.; Tanaka, Y.; Tsuda, S.; Kambe, N.; Taniguchi, M.; Kawai, T.; Saeki, A.; Seki, S. Insulated
612 molecular wire with highly conductive π–conjugated polymer core. *J. Am. Chem. Soc.* **131**, 18046–
613 18047 (2009).

614 37. Masai, H.; Yokoyama, T.; Miyagishi, H. V.; Liu, M.; Tachibana, Y.; Fujihara, T.; Tsuji, Y.; Terao, J.
615 Insulated conjugated bimetallopolymer with sigmoidal response by dual self-controlling system as a
616 biomimetic material. *Nat. Commun.* **11**, 408 (2020).

617 38. Masai, H.; Terao, J. Stimuli-responsive functionalized insulated conjugated polymers. *Polym. J.* **49**,
618 805–814 (2017).

619 39. Hosomi, T.; Masai, H.; Fujihara, T.; Tsuji, Y.; Terao, J. A typical metal-ion-responsive color-tunable
620 emitting insulated π-conjugated polymer film. *Angew. Chem. Int. Ed.* **55**, 13427–13431 (2016).

621 40. Masai, H.; Terao, J.; Makuta, S.; Tachibana, Y.; Fujihara, T.; Tsuji, Y. Enhancement of
622 phosphorescence and unimolecular behavior in the solid state by perfect insulation of platinum–
623 acetylide polymers. *J. Am. Chem. Soc.* **136**, 14714–14717 (2014).

624 41. Masai, H.; Terao, J.; Seki, S.; Nakashima, S.; Kiguchi, M.; Okoshi, K.; Fujihara, T.; Tsuji, Y. Synthesis
625 of one-dimensional metal-containing insulated molecular wire with versatile properties directed
626 toward molecular electronics materials. *J. Am. Chem. Soc.* **136**, 1742–1745 (2014).

42. Queffélec, C.; Petit, M.; Janvier, P.; Knight, D. A.; Bujoli, B. Surface modification using phosphonic acids and esters. *Chem. Rev.* **112**, 3777–3807 (2012).

43. Kalek, M.; Jezowska, M.; Stawinski, J. Preparation of arylphosphonates by palladium(O)-catalyzed cross-coupling in the presence of acetate additives: synthetic and mechanistic studies. *Adv. Synth. Catal.* **351**, 3207–3216 (2009).

44. Motion of threading/dethreading transformation is shown in Fig. S1 in the supporting information.

45. Chou, S.-Y.; Masai, H.; Tsuda, S.; Terao, J. Synthetic methodology for structurally defined and insulated molecular wires bearing non-centrosymmetric conjugated axle components via iterative intramolecular slippage. *Chem. - An Asian J.* **14**, 1667–1671 (2019).

46. Masai, H.; Terao, J. Synthetic methodologies for structurally defined linked-[n]rotaxanes with permethylated cyclodextrins: platform for functionalized molecular electronics. *Bull. Chem. Soc. Jpn.* **92**, 529–539 (2019).

47. Nishiyabu, R.; Kano, K. Double self-inclusion by rotating glucopyranose units in per-*O*-methylated β-cyclodextrin moieties attached to a porphyrin in aqueous solution. *European J. Org. Chem.* No. 24, 4985–4988 (2004).

48. Masai, H.; Terao, J.; Fujihara, T.; Tsuji, Y. Rational design for rotaxane synthesis through intramolecular slippage: control of activation energy by rigid axle length. *Chem. - A Eur. J.* **22**, 6624–6630 (2016).

49. Ohta, H.; Orita, M.; Hirano, M.; Hosono, H. Surface morphology and crystal quality of low resistive indium tin oxide grown on yittria-stabilized zirconia. *J. Appl. Phys.* **91**, 3547–3550 (2002).

50. Ohta, H.; Kambayashi, T.; Hirano, M.; Hoshi, H.; Ishikawa, K.; Takezoe, H.; Hosono, H. Application of transparent conductive substrate with atomically flat & stepped surface for lateral growth of organic molecule: vanadyl-phthalocyanine. *Adv. Mater.* **15**, 1258–1262 (2003).

51. AFM underestimated the absolute height of **3** immobilized on the surface of a single-crystalline ITO because of the softness of **3** and the interaction between the AFM probe and sample surface according to the following references: (a) Jiao, Y.; Schäffer, T. E. Accurate height and volume measurements on soft samples with the atomic force microscope. *Langmuir* **20**, 10038–10045 (2004). (b) Ebenstein, Y.; Nahum, E.; Banin, U. Tapping mode atomic force microscopy for nanoparticle sizing: tip-sample interaction effects. *Nano Lett.* **2**, 945–950 (2002).

52. Steentjes, T.; Jonkheijm, P.; Huskens, J. Electron transfer processes in ferrocene-modified poly(ethylene glycol) monolayers on electrodes. *Langmuir* **33**, 11878–11883 (2017).

53. Eckermann, A. L.; Feld, D. J.; Shaw, J. A.; Meade, T. J. Electrochemistry of redox-active self-assembled monolayers. *Coord. Chem. Rev.* **254**, 1769–1802 (2010).

54. Elgrishi, N.; Rountree, K. J.; McCarthy, B. D.; Rountree, E. S.; Eisenhart, T. T.; Dempsey, J. L. A practical beginner's guide to cyclic voltammetry. *J. Chem. Educ.* **95**, 197–206 (2018).

55. Bard, A. J.; Faulkner, R. L. *Electrochemical Methods: Fundamentals and Applications, 2nd Ed.* (John Wiley & Sons, 2001).

56. Tian, H.; Dai, Y.; Shao, H.; Yu, H. Z. Modulated intermolecular interactions in ferrocenylalkanethiolate self-assembled monolayers on gold. *J. Phys. Chem. C* **117**, 1006–1012 (2013).

57. Hanna, C. M.; Luu, A.; Yang, J. Y. Proton-coupled electron transfer at anthraquinone modified indium tin oxide electrodes. *ACS Appl. Energy Mater.* **2**, 59–65 (2019).

58. Guo, Y.; Zhao, J.; Zhu, J. Study on the intermolecular interactions between the functional moieties in ferrocene-terminated alkanethiol self-assembled monolayer on gold. *Thin Solid Films* **516**, 3051–3057 (2008).

59. Laviron, E. General expression of the linear potential sweep voltammogram in the case of diffusionless electrochemical systems. *J. Electroanal. Chem.* **101**, 19–28 (1979).

673 60. Wang, L.; Polyansky, D. E.; Concepcion, J. J. Self-assembled bilayers as an anchoring strategy:
674 catalysts, chromophores, and chromophore-catalyst assemblies. *J. Am. Chem. Soc.* **141**, 8020–8027
675 (2020).

676 61. Kiguchi, M.; Nakashima, S.; Tada, T.; Watanabe, S.; Tsuda, S.; Tsuji, Y.; Terao, J. Single-molecule
677 conductance of π-conjugated rotaxane: new method for measuring stipulated electric conductance of
678 π-conjugated molecular wire using STM break junction. *Small* **8**, 726–730 (2012).

679 62. Zhang, B.; Sun, L. Artificial photosynthesis: opportunities and challenges of molecular catalysts. *Chem.*
680 *Soc. Rev.* **48**, 2216–2264 (2019).

681 63. Wang, J. C.; Violette, K.; Ogunsolu, O. O.; Hanson, K. Metal ion mediated electron transfer at dye-
682 semiconductor interfaces. *Phys. Chem. Chem. Phys.* **19**, 2679–2682 (2017).

683 64. Han, N.; Wang, Y.; Ma, L.; Wen, J.; Li, J.; Zheng, H.; Nie, K.; Wang, X.; Zhao, F.; Li, Y.; Fan, J.;
684 Zhong, J.; Wu, T.; Miller, D. J.; Lu, J.; Lee, S.t-T.; Li, Y. Supported cobalt polyphthalocyanine for
685 high-performance electrocatalytic CO_2 reduction. *Chem* **3**, 652–664 (2017).

686 65. Dalle, K. E.; Warnan, J.; Leung, J. J.; Reuillard, B.; Karmel, I. S.; Reisner, E. Electro- and solar-driven
687 fuel synthesis with first row transition metal complexes. *Chem. Rev.* **119**, 2752–2875 (2019).

688 66. Chemical structure of **S12**:

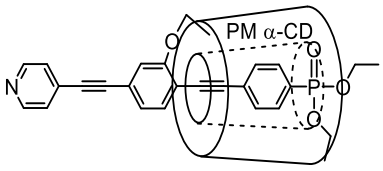

689

690 67. Mase, K.; Ohkubo, K.; Fukuzumi, S. Efficient two-electron reduction of dioxygen to hydrogen
691 peroxide with one-electron reductants with a small overpotential catalyzed by a cobalt chlorin complex.
692 *J. Am. Chem. Soc.* **135**, 2800–2808 (2013).

693 68. Formation of μ-1,2-peroxo dinuclear structure.

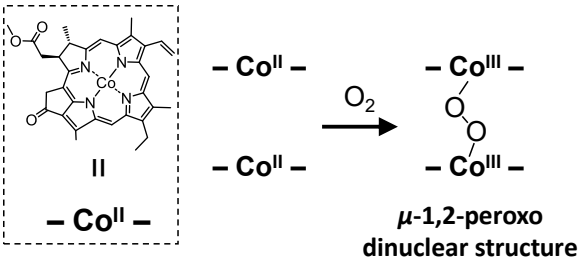

69. Mase, K.; Yoneda, M.; Yamada, Y.; Fukuzumi, S. Seawater usable for production and consumption of hydrogen peroxide as a solar fuel. *Nat. Commun.* **7**, 11470 (2016).

70. Complex formation between **S12** and **Co^{II}(Ch)** was confirmed by ^{1}H NMR and the evidence is shown in Figure S11.

Acknowledgements

The authors would appreciate Shunichi Kaneko, Hiroki Hirano, and Yuichi Yasutake for their investigation for the preliminary results. This research was supported by financial supports (JSPS KAKENHI Grant Numbers 18H05158 in Scientific Research on Innovative Areas "Innovations for LightEnergy Conversion (I4LEC)", 19H02696, 19K22179, and 19K15629, JST CREST Grant Number JPMJCR1331). This work was performed under the Cooperative Research Program of "Network Joint Research Center for Materials and Devices".

Ethics declarations

Competing interests

The authors declare no competing interests.

Supplementary Information

Supplementary information is available for this paper at

Supplementary Files

This is a list of supplementary files associated with this preprint. Click to download.

- SI.pdf